**Climate
of the Past
Discussions**

Upper ocean climate of the Eastern Mediterranean Sea during the Holocene Insolation Maximum – a model study

F. Adloff[1,2], U. Mikolajewicz[1], M. Kucera[3], R. Grimm[1,2], E. Maier-Reimer[1],
G. Schmiedl[4], and K. Emeis[5]

[1]Max Planck Institute for Meteorology, Hamburg, Germany
[2]International Max Planck Research School on Earth System Modelling, Hamburg, Germany
[3]Univ Tübingen, Department of Geosciences, Tübingen, Germany
[4]Department of Geosciences, University of Hamburg, Hamburg, Germany
[5]Univ Hamburg, Inst Biogeochem and Marine Chem, Hamburg, Germany

Correspondence to: F. Adloff (fanny.adloff@zmaw.de)

CPD

7, 1457–1509, 2011

Early Holocene ocean climate of the Eastern Mediterranean

F. Adloff et al.

Title Page	
Abstract	Introduction
Conclusions	References
Tables	Figures

◀◀	▶▶
◀	▶
Back	Close

Full Screen / Esc

Printer-friendly Version

Interactive Discussion

Abstract

Nine thousand years ago, the Northern Hemisphere experienced enhanced season-ality caused by an orbital configuration with a minimum of the precession index. To assess the impact of the "Holocene Insolation Maximum" (HIM) on the Mediterranean
Sea, we use a regional ocean general circulation model forced by atmospheric input derived from global simulations. A stronger seasonal cycle is simulated in the model, which shows a relatively homogeneous winter cooling and a summer warming with well-defined spatial patterns, in particular a subsurface warming in the Cretan and Western Levantine areas.

The comparison between the SST simulated for the HIM and the reconstructions from planktonic foraminifera transfer functions shows a poor agreement, especially for summer, when the vertical temperature gradient is strong. However, a reinterpretation of the reconstructions is proposed, to consider the conditions throughout the upper water column. Such a depth-integrated approach accounts for the vertical range of preferred habitat depths of the foraminifera used for the reconstructions and strongly improves the agreement between modelled and reconstructed temperature signal. The subsurface warming is recorded by both model and proxies, with a light shift to the south in the model results.

The mechanisms responsible for the peculiar subsurface pattern are found to be a combination of enhanced downwelling and wind mixing due to strengthened Etesian winds, and enhanced thermal forcing due to the stronger summer insolation in the Northern Hemisphere. Together, these processes induce a stronger heat transfer from the surface to the subsurface during late summer in the Western Levantine; this leads to an enhanced heat piracy in this region.

1   Introduction

During the early Holocene, the Northern Hemisphere climate experienced an enhanced seasonality of insolation. This period is referred to the Holocene Insolation Maximum (HIM) because of the high insolation rate occurring in Northern Hemisphere
5   summer. The stronger seasonality of the insolation was associated with a strengthening of the North African monsoon (e.g., Rossignol-Strick, 1983).

Coinciding with this time period, sediment cores from the Eastern Mediterranean Sea display a dark sediment layer, rich in organic carbon, called sapropel S1, deposited between approximately 9000 and 6000 yr BP (e.g., Mercone et al., 2000). The sapropel
10   S1 and earlier equivalents reflect low oxygen availability in the deep Eastern Mediterranean Basin. One of the hypothesis for the sapropel formation is that both warming and freshening of the Mediterranean surface water induced a decrease in surface density and thus prevented the ventilation of deeper layers through the reduced/absent formation of dense deep water, promoting the preservation of organic matter in the
15   sediment (e.g., Rohling and Hilgen, 1991; Rohling, 1994; Cramp and O'Sullivan, 1999).

Because of its isolated configuration, the Mediterranean Sea, as a "mini-ocean", is thought to show a rapid and amplified response to past or future climate changes and can be used as a "laboratory" for modelling climate changes. However, only few paleo-modelling studies have investigated the effect of changes in atmospheric forcing on
20   the Mediterranean. Both Bigg (1994) and Mikolajewicz (2011) used a regional ocean general circulation model (OGCM) forced by fluxes interactively calculated from bulk formulas with atmospheric input data from a coarse resolution atmospheric model to simulate the ocean climate of the Last Glacial Maximum (LGM) for the Mediterranean. Meijer and Tuenter (2007) forced their OGCM with present-day realistic climate, and
25   adjusted the runoff and precipitation minus evaporation ($P - E$) values to precession minimum conditions; those adjustments were based on experiments performed with an Earth system model of intermediate complexity. Myers et al. (1998) and Myers and Rohling (2002) forced a regional OGCM with both modified sea surface temperature (SST) and salinity (SSS) according to reconstructions. Their studies focused on the

LGM and the early Holocene. Meijer and Dijkstra (2009) forced their regional OGCM with strongly idealized atmospheric forcing to mimic the effect of a past climate change.

Our modelling strategy aims at simulating the Mediterranean ocean climate at sapropel time and to investigate the sensitivity of the ventilation of the deep Eastern Mediterranean to various climate perturbations. In this paper, we focus as a first step of this strategy on the analysis and validation of baseline simulations of the HIM climate (9000 yr BP) as a representation of the pre-sapropel S1 well-ventilated state. In a future study, we will perform perturbation experiments and assess the plausible physical mechanisms leading to a weakening of the ventilation.

The present study aims at investigating the changes in ocean climate that are simulated in response to an atmospheric forcing representing the HIM. The focus lies on the upper ocean of the Eastern Mediterranean. A newly compiled data set of reconstructed upper-ocean temperature (see Kucera et al., 2011) allows us to validate the model simulations and to analyze the causes for some of the climate changes found in this data set.

For this purpose of course, the model has to be free from any information from paleo-reconstructions. We therefore follow a similar approach as the one used by Bigg (1994) and Mikolajewicz (2011) by using a regional OGCM which is forced by fluxes calculated with bulk formulas from atmospheric input data derived from long-term simulations with a coupled global atmosphere-ocean-vegetation model.

The goals of this study are the following: (1) to analyze the modelled changes in the upper-ocean state during the "Holocene Insolation Maximum", (2) to investigate the physical mechanisms responsible for strong regional contrasts of the modelled temperature signal, (3) to validate the modelling results with sea surface temperature reconstructions.

The paper is organized as follows: in Sect. 2 model, forcing and experiments are described. Key quantities of the obtained model control climate are compared to observations in Sect. 3. The results for the HIM are described, analyzed and compared to observations in Sect. 4.

Early Holocene ocean climate of the Eastern Mediterranean

F. Adloff et al.

|◄ | ►|

◄ | ►

Back | Close

Full Screen / Esc

Printer-friendly Version

Interactive Discussion

2 Model, forcing and experiments

2.1 The regional OGCM

For this study, we use the Mediterranean configuration of the ocean general circulation model MPI-OM (Max-Planck-Institute Ocean Model) (Mikolajewicz, 2011). The physics
[5] of the model is described in Marsland et al. (2003). The model grid covers the entire Mediterranean Sea including the Black Sea and a small area of the Atlantic, west of Gibraltar (Fig. 1). The grid is curvilinear with an horizontal resolution of roughly 20 km. We use a 29-level z-coordinates system, with 5 levels within the upper 50 m. The thickness of the first ocean layer is 12 m, the model SST is thus centered at 6 m depth.
[10] The time step is 36 min.

The topography is realistic, the Strait of Gibraltar and the Bosphorus are both represented by one grid point and their sills have depths of 256 and 21 m, respectively in the topography used for the pre-industrial climate simulation. During the early Holocene, the sea level was 20 m lower than today. To account for this in the paleo-simulations,
[15] we reduced the depth by modifying the Mediterranean Sea topography according to the ICE-5G reconstruction from Peltier (2004) (Fig. 1). Moreover, we assume the Bosphorus to be closed at this time, so that there is no outflow of fresher water from the Black Sea into the Marmara Sea. We base this assumption on the study from Ryan et al. (1997) who consider a catastrophic inflow of water from Mediterranean into Black
[20] Sea happening around 8.4 ky BP, and the study from Sperling et al. (2003) who reconstructed high salinities in the Marmara Sea for S1 sapropel time. However, other studies contradict this statement; Aksu et al. (2002), for instance, suggests an overflow from Black Sea into the Marmara Sea from 10.5 ky BP onwards with low salinities found in the Marmara Sea.

Early Holocene ocean climate of the Eastern Mediterranean

F. Adloff et al.

2.2   Atmospheric forcing and boundary conditions

At the surface, the Mediterranean regional OGCM is forced by air-sea fluxes of heat, momentum and water. The heat fluxes are calculated with bulk formulas from daily atmospheric data.

⁵   The atmospheric forcing is derived from long-term simulations performed with the coupled global circulation model ECHAM5/MPI-OM/LPJ in a global setup (Mikolajew-icz et al., 2007). The atmosphere component ECHAM5 (Roeckner et al., 2003) has a T31 horizontal resolution and 19 vertical levels; the ocean component MPI-OM has a curvilinear grid with poles over Greenland and Antarctica. The horizontal resolution

¹⁰ of MPI-OM is roughly 3°, and there are 40 vertical levels. The dynamical vegetation component LPJ has the same horizontal resolution as the atmosphere component.

2.2.1   Global model setup

The simulations with the global model have been carried out until equilibrium for the pre-industrial climate and for two different simulations of the HIM. For the pre-industrial

¹⁵ global simulation, the insolation corresponds to 1950 and the atmospheric partial pressure of CO_2 (pCO_2) is 280 ppm. For the HIM (9 ky BP), the global simulation used to force the "9K1" regional simulation only considers changes in insolation. In the HIM global simulation used to force the "9K2" regional simulation, besides the changes in earth orbital parameters, the atmospheric pCO_2 is set to 260 ppm instead of 280 ppm

²⁰ and the topography is modified using ice sheet distributions and topography changes according to the ICE-5G reconstruction (Peltier, 2004).

     From these global simulations, we derived three different sets of atmospheric forcing input: one for the pre-industrial climate used as control climate (CTRL) and two for the HIM climate (9K1 and 9K2).

²⁵   We extracted a 100-yr daily atmospheric forcing data set with the following variables: precipitation, incoming short wave radiation, cloud cover, near-surface air temperature, dew point temperature, 10-m wind speed and sea level pressure. Due to the coarse

resolution of the global coupled model, simulated wind stress patterns are too smooth over the Mediterranean Sea.

Therefore, we applied a statistical downscaling to calculate the wind stress from the sea level pressure (SLP) of the global model. For the statistical downscaling, a statisti-
5   cal relation between principal component time series of empirical orthogonal functions (EOFs, von Storch and Zwiers, 1999) of daily data of SLP of the Mediterranean and adjacent regions (truncated on the T31-grid of the global model), and wind stress interpolated onto the ocean model grid was estimated by linear regression using NCEP reanalysis data for the period 1978–2002 (Kalnay et al., 1996). The long-term mean
10 was subtracted from all data prior to the analysis. Afterward, SLP anomalies from the coarse resolution global model were projected onto the EOFs. Wind stress anomalies were estimated from the obtained loadings using the regression matrix obtained from the NCEP reanalysis and added to the long-term mean obtained from NCEP reanalysis.
15 As the global model has a cold bias over the Mediterranean, the systematic bias between the model and the NCEP climatology was added to the actual model values for near-surface air temperature and dew point temperature

2.2.2   Fresh water fluxes and restoring

The components of the water fluxes are the monthly prescribed river runoff (R), the pre-
20 cipitation (P) from the atmospheric data derived from the global model, and the evaporation (E) calculated from the latent heat flux using model SST. For the river discharge, we use a 1-yr monthly climatology from the UNESCO RivDis database (Vörösmarty et al., 1998). The seasonal cycle is taken into account only for the major rivers (Danube, Nile, Dniepr, Rhone, Po and Ebro). For the Nile and the Ebro rivers, we consider dis-
25 charge rates prior to the damming, with a yearly averaged runoff of $2930\,\mathrm{m^3\,s^{-1}}$ for the Nile and $410\,\mathrm{m^3\,s^{-1}}$ for the Ebro. For the HIM simulations, the anomalies (9K vs. CTRL) of the river discharge simulated by the coupled model are superimposed on the monthly climatology of river runoff used for the CTRL experiment.

Title Page

Abstract | Introduction

Conclusions | References

Tables | Figures

|◀ | ▶|

◀ | ▶

Back | Close

Full Screen / Esc

Printer-friendly Version

Interactive Discussion

At the surface, there is no restoring to SST and SSS. At the western margin of the Atlantic box, a restoring to climatological monthly temperature and salinity from World Ocean Atlas (WOA, Levitus et al., 1998) is applied over 5 grid cells. For the paleo-simulations, the same procedure is applied as for the runoff: the anomalies (9K vs. CTRL) of the Atlantic hydrography from the global model experiments are superimposed to the values used in CTRL.

The evaporation is varying, depending on the latent heat flux, which is a function of the SST. As the freshwater fluxes also affect sea level due to the mass flux boundary condition, the net evaporation of the Mediterranean would lead to continuously decreasing sea level. To account for this, we perform a sea level restoring in the 5 most western grid cells of the Atlantic buffer zone, thus ensuring that the net water transport through the Strait of Gibraltar corresponds to the net water loss in the Mediterranean and the Black Sea.

2.3 Spin-up and initial conditions

The integration time strongly differs between the already existing studies: 25 yr for Bigg (1994), 20 yr for Meijer and Tuenter (2007), 100 yr for Myers et al. (1998) and Myers and Rohling (2002), 1000 yr for Meijer and Dijkstra (2009) and 1999 yr for Mikolajewicz (2011). A long spinup is essential to reach an ocean state which is no longer drifting from the surface to intermediate depths and we therefore perform 700 yr simulations with the Mediterranean OGCM.

We start the three simulations from an initial state with homogeneous low density water (38 psu and 20 °C for the Mediterranean and the Atlantic box; 20 psu and 20 °C for the Black Sea) and let the model run in a free mode for 700 yr, forced by the 100-yr daily atmospheric dataset repeated in a loop. Such initial conditions allow the model to form its own water masses without being under the influence of starting hydrographic conditions derived from a climatology. The results presented in this study correspond to an annual climatology based on the last 100 yr (years 601 to 700).

3 The general features of the Eastern Mediterranean Sea for the control climate

3.1 Near-surface circulation and deep water formation

The circulation features of the Eastern Mediterranean Sea for the CTRL climate are illustrated in Fig. 2 by the near-surface currents field at 27 m depth. Two intense cyclonic gyres are represented in the Adriatic and in the North Levantine Basin (Rhodes Gyre). These gyres correspond to the location of dense water formation. Consistently with the description of the horizontal circulation structure summarized by Pinardi and Masetti (2000), the Atlantic-Ionian Stream coming from the Atlantic Ocean and entering through the Strait of Sicily into the Central Ionian is well-simulated, as are the Mid-Mediterranean Jet flowing between Crete and the North African coast and the Asia Minor Current flowing along the Turkish coasts.

Linked to this general circulation, the winter mixed layer depth is an indicator widely used to assess the ability of a model to form the different Mediterranean water masses. Figure 2 shows that deep mixed layer patterns are modelled in the Adriatic, where the Adriatic Bottom Water (ABW) is formed and flows out of the Otranto Strait, in the South Aegean Sea and in the North Levantine where the Levantine Intermediate Water (LIW) is formed. In the Ionian Sea, the mixing of transformed LIW with outflowing ABW forms the Eastern Mediterranean Deep Water (EMDW). The modelled mixed layer patterns are realistic and consistent with the climatology of D'Ortenzio et al. (2005) based on observations and calculated with a temperature difference criterion.

The model simulates an averaged net water transport at Gibraltar of 0,051 Sv (1 Sv = $10^6\,\mathrm{m}^3\,\mathrm{s}^{-1}$), with a surface inflow of 0.84 Sv and a deep outflow of 0.79 Sv. Those values are in agreement with observations by Bryden and Kinder (1991); Bryden et al. (1994); Tsimplis and Bryden (2000) and Baschek et al. (2001), who suggest values between 0.72 and 0.92 Sv for the inflow and between 0.68 and 0.88 Sv for the outflow. The modelled LIW transport at the Sicily Strait from the eastern basin to the western basin occurs below 120 m depth and has a mean value around 1.04 Sv which is very close to the observed value of 1.1 Sv (Garzoli and Maillard, 1979; Astraldi et al., 1996).

3.2 Surface temperature and salinity

To assess the ability of the model to reproduce observed SST and SSS patterns, we compare our results from the CTRL simulation with the climatologies from WOA 1998 (Levitus et al., 1998) and MEDATLAS (MEDAR-Group, 2002). Because the tempera-
5 ture point in our model vertical discretization is at 6 m depth, we consider the climatological temperature interpolated to 6 m depth to make a consistent comparison.

Figure 3 shows the comparison between the modelled and both climatological SSTs. The model exhibits SST gradient from west to east and from north to south, consistently with the climatologies. For the annual mean as well as for winter (JFM) SST, the de-
10 viations remain below 1 K. The winter modelled SST values are in between the values of both climatologies, MEDATLAS showing slightly warmer SST than WOA in the Levantine Sea and in the Southern Ionian Sea. For the summer (JAS) SST, WOA displays SST 1 to 2 K warmer than MEDATLAS. The modelled summer SST shows warm biases in comparison with both climatologies. In the Southern Ionian Sea and in the Eastern
15 Levantine Sea, biases up to 3 K are simulated by the model (in comparison with MEDATLAS, the coldest climatology). These biases could be due to the Atlantic-Ionian jet travelling slightly too far north in the model (compared to Pinardi and Masetti, 2000), thus reducing the import of cooler water from the western basin into the Southern Ionian Sea. Both the Aegean and Adriatic Seas have too cold simulated temperatures
20 during winter time. These regions are almost land-locked, with narrow connections to the wider part of the Eastern Mediterranean, through the Strait of Otranto for the Adriatic Sea and three straits of the Cretan Arc for the Aegean Sea. Small-scale atmospheric processes are acting over both areas, so that accurate wind patterns are difficult to simulate adequately at the resolution we are using.
25 Figure 4 displays the deviations of the annual mean modelled SSS from both MEDATLAS and WOA climatologies. The comparison of model results with each climatology exhibits similar discrepancies, which are found in the Levantine and in the Cretan region with a salty bias around 0.3 psu. The fresh bias in the Northern Aegean indicates

that the model overestimates the fresh water input in this region. The northern part of the Adriatic Sea has a strong negative salinity anomaly corresponding to the fresh tongue from the Po river runoff that flows along the western coast. Nevertheless, the Central and South Adriatic show a strong salty bias up to 0.5 psu which can be linked to the underestimation of the mean fresh water input from the Adriatic rivers as well as the overestimation of the penetration of salty Ionian water into the Adriatic. However, part of this discrepancy is probably artificial, as it can be attributed to the smoothing of the observational data, which has been introduced in the generation of the observational climatologies. Finally, the model has a positive salinity bias all along the North African coast. There are several contributors to this bias: first, this area has a warm SST bias (probably linked to the inability of the model to represent small scale atmospheric processes at the coasts, as explained before), leading to a stronger evaporation and consequently higher salinities. Second, the regional river discharge may be underestimated; third, the Atlantic-Ionian jet, which brings fresher water to the eastern basin, is located slightly too far north in the model. Thus, the Southern Ionian remains somewhat isolated and is not significantly impacted by this fresher current. Most of the discrepancies do not reflect the inadequacy of the model to correctly simulate consistent SSS, but they can be directly linked to some discrepancies in the fresh water components of our forcing, mainly the too low precipitation (explained hereafter) as well as missing river discharge. On average, this induces an averaged positive salinity bias of 0.25 psu in the eastern basin.

3.3 Water budget

Table 1 summarizes the different components of the fresh water budget for the Mediterranean. The averaged precipitation prescribed over the Mediterranean Sea from the global models only $0.59\,\mathrm{mm\,day^{-1}}$ and the averaged calculated evaporation is $2.83\,\mathrm{mm\,day^{-1}}$. The rivers contribute to the fresh water input by adding $0.35\,\mathrm{mm\,day^{-1}}$. The input from the rivers is close to the data from Ludwig et al. (2009), who indicate a value of $0.39\,\mathrm{mm\,day^{-1}}$. Nevertheless, the amount of prescribed precipitation

is relatively low in comparison with both observations and reanalysis (0.7 mm day^{-1} for HOAPS, Andersson et al., 2007; and 1.07 mm day^{-1} for ERA-Interim Reanalysis, Simmons et al., 2007). The interactively calculated evaporation is also lower than values from reanalysis (3.34 mm day^{-1} for ERA-Interim Reanalysis and observations (3.12 mm day^{-1} for HOAPS).

The resulting water deficit of 1.89 mm day^{-1} is compensated by the positive net fresh water transport from the Black Sea into the Mediterranean through the Strait of the Dardanelles (0.18 mm day^{-1} or 0.0055 Sv) and from the Atlantic Ocean through the Strait of Gibraltar (1.71 mm day^{-1} or 0.051 Sv). The net water transport through both straits is consistent with the obervations. Bryden et al. (1994), Bryden and Kinder (1991) and Béthoux (1979) suggest the values of 1.42 mm day^{-1}, 1.37–1.64 mm day^{-1} and 2.74 mm day^{-1}, respectively for the estimation of the net water transport at Gibraltar. Concerning the net water transport from the Black Sea through the Dardanelles Strait, the data from Stanev and Peneva (2002) indicate a value of 0.22 mm day^{-1}.

In Table 1, we compare the mean values of each component of the water budget averaged for the full Mediterranean with those averaged for the eastern basin only (from the Strait of Sicily until the Bosphorus). This shows how much the eastern basin differs from the western in terms of $E - P$ balance. We observe that the mean precipitation rate in the eastern basin is around 25 % lower than for the full basin, the mean river input is 65 % lower and the mean evaporation is 7 % higher. The Nile is responsible for 80 % of the river input of the eastern basin.

4 The Holocene Insolation Maximum

4.1 Stronger seasonal cycle

In the HIM global simulations, the changes in the Earth's orbital parameters lead to stronger amplitude of the seasonal cycle of insolation. The averaged downward short wave radiation at the top of the atmosphere over the Mediterranean Sea is increased by about 15 Wm^{-2} during the summer season and is decreased by about 15.5 Wm^{-2}

during the winter season for both 9K1 and 9K2 experiments in comparison with the CTRL experiment. This leads to an increased summer warming and an enhanced winter cooling as shown by the near-surface air temperature anomalies signal displayed in Fig. 5. The more realistic set up in 9K2 (presence of the decaying Laurentide ice sheet and lower atmospheric pCO$_2$) leads to a generally slightly colder climate in 9K2. This decreases the summer warming and increases the winter cooling in comparison with the 9K1 simulation.

The increase in the amplitude of the seasonal cycle of solar forcing during the HIM is associated with an increase in P. In winter, P is enhanced over the basin due to a more southerly propagation of cyclones. In summer, the intensified North African monsoon is responsible for enhanced P over the Levantine Sea. This overcompensates the water loss from the increased summer E in this area, thus inducing positive values of $P - E$ (Fig. 6). In the rest of the basin, the increase in P is not sufficient to compensate the increased E, leading to negative values of $P - E$. The Nile has a larger water discharge for the HIM with runoff surplus of 4564 m^3 s^{-1} for the 9K1 simulation and 2471 m^3 s^{-1} for the 9K2 simulation in comparison with the CTRL experiment.

Table 1 summarizes each component of the water budget for the CTRL and the two HIM simulations over sea, for the entire Mediterranean and for the Eastern Mediterranean (the western boundary at the Strait of Sicily). If we consider the entire Mediterranean, the precipitation over sea remains almost constant for the 9K2 simulation but we see an increase by 12 % for the 9K1 simulation. The evaporation is almost unchanged. The total riverine fresh water input is increased by more than 40 % for the 9K1 simulation and more than 20 % for the 9K2 simulation. In both cases, the increase is mainly due to the enhanced discharge from the Nile river which is directly linked to the increased North African monsoon. If we consider the eastern basin only, the increase in precipitation is higher with a value of 20 % for the 9K1 simulation and can be neglected for 9K2. The changes in evaporation are small for both simulations.

The fresh water input from the river runoff into the Eastern Mediterranean is almost doubled for the 9K2 simulation and enhanced by a factor of 2.5 for the 9K1 simulation;

in both cases the enhanced Nile runoff is the main contributor to this increase. Mainly because of the enhanced riverine input, the $P + R - E$ value over the Eastern Mediterranean decreases during the HIM. This lowered the net water transport between the western and the eastern basins.

5   In general, the fresh water budget shows relatively little changes because the enhanced Nile runoff overcompensates the missing water from the Black Sea.

4.2   Near-surface circulation and deep water formation

As a consequence of the missing outflow from the Black Sea due to the closure of the Bosphorus in the HIM simulations, salinity in the Aegean Sea increases (Fig. 7).
10   This results in a shift of the location of intermediate water formation from the North Levantine/South Aegean towards the North Aegean (Fig. 7) as shown by the proxy-based study of Schmiedl et al. (2010) which implies a persistent deep water ventilation in the Northern Aegean Sea during the HIM. In our simulations, the salty and relatively dense water formed in this region flows out of the Aegean Sea through the Antikithira
15   Strait and follows the Western Greek coast towards the Adriatic. Along the trajectory following Western Greece, a mixed layer pattern of intermediate depth appears due to the fact that the dense salty water flowing from the Aegean entrains the surrounding lighter water on its way to the Adriatic.

   In the 9K2 simulation, the salinity is approximately 0.2 psu higher than in 9K1 and
20   CTRL. The main cause is the higher salinity of the inflowing Atlantic water (due to the lower sea level in the corresponding global simulation, global mean salinity is higher). The enhanced discharge of the Nile tends to reduce the salinity. The latter effect is stronger in 9K1 than in 9K2.

   However, the observed mixed layer depth patterns remain similar in both simulations.

Early Holocene ocean climate of the Eastern Mediterranean

F. Adloff et al.

Back | Close

Full Screen / Esc

Printer-friendly Version

Interactive Discussion

Discussion Paper | Discussion Paper | Discussion Paper | Discussion Paper

Title Page

Abstract Introduction

Conclusions References

Tables Figures

◄◄ ►►

◄ ►

Back Close

Full Screen / Esc

Printer-friendly Version

Interactive Discussion

4.3 The upper-ocean temperature

4.3.1 Seasonal cycle

As a direct effect of the changes in incoming short wave radiation at the surface, an increase in the amplitude of the seasonal cycle of the water temperature (Fig. 8) is simulated. The enhanced cooling during winter spreads over the entire water column through mixing and convective processes. The enhanced seasonal cycle leads to warmer surface temperatures in both 9K simulations in summer. During spring and summer, stable stratification prevents a deep penetration of the warming signal. The region with temperatures warmer than in the control run is thus restricted to the upper 30 and 20 m, respectively for the 9K1 and 9K2 simulations. Since the 9K1 simulation is in general warmer than the 9K2 simulation (due to the presence of rest of the Laurentide ice sheet and reduced atmospheric pCO$_2$ in 9K2), the summer warming relative to the CTRL run is more intense (up to +1.5 K for the surface water of the 9K1 experiment vs. +0.8 K for 9K2) and spreads slightly deeper than for the 9K2. Below, the water shows cold anomalies during summer, which is a remainder from the cold winter signal.

4.3.2 The Western Levantine subsurface warming pattern

In this section, we analyze the patterns of the spread of the surface summer warming signal into the subsurface layers. Figure 9 displays the anomalies between 9K1/9K2 and the CTRL, for 6 m depth (the modelled SST), 17 m depth and 27 m depth. The surface warming is relatively homogeneous for both paleo-simulations, but the subsurface temperature anomaly signal shows strong regional contrasts with a well-defined pattern. At 17 m depth, the region around Crete and the Western Levantine still shows a warming signal, whereas the Central Ionian, the Tyrrhenian and, only for 9K1, the Eastern Levantine, experience a cooling. At 27 m depth, cooling is mainly observed

over the Eastern Mediterranean, but is strongly reduced around Crete and Western Levantine, and even absent for the 9K1 simulation.

The pattern of subsurface temperature anomalies is quite similar to the present-day pattern of subsurface spread of the summer SST in the Eastern Mediterranean (Fig. 10). The model shows weaker vertical gradients of the near-surface temperature in the Western Levantine (and thus a deeper penetration of the summer warming signal) than in the Eastern Levantine and the Ionian; the same pattern is also obvious in the MEDATLAS climatology.

This can be explained by the Etesian winds. The Etesian winds are dry northerly winds blowing over the Aegean Sea and the Levantine Sea from about mid-May to mid-September, mainly because of the monsoon effect leading to a thermal low pressure trough over Turkey, with higher pressure over Southern Balkans; and the passage of cold fronts over the Balkans and the associated cold-air circulation behind them (e.g., Meteorological-Office, 1962; Brody and Nestor, 1985). In the model derived forcing used for CTRL, Etesian winds are acting from mid-May until mid-October (Fig. 11, black line) and are essentially a north-south blowing wind (Figs. 11 and 12). The westward Ekman transport induced by this wind pattern involves upwelling of cold subsurface water in the Eastern Levantine (resulting in a strong vertical near-surface temperature gradient) and downwelling of warm surface water west of the core of the Etesian winds with reduced vertical near-surface temperature gradient. As an example, the vertical velocities and the associated subsurface heating rates are displayed in Fig. 13. The westward Ekman transport leads to a substantial heat transport from the Eastern to the Western Levantine. This becomes evident when comparing the atmospheric heat input with the actually observed changes in ocean heat content for the period from May to September, when the Etesian winds are present (Fig. 14, left). In the Western Levantine, an additional heat source of up to $60\,\mathrm{Wm}^{-2}$ working for 5 months is required to explain the changes in ocean temperature. In the Eastern Levantine, a similar heat sink is required (up to $65\,\mathrm{Wm}^{-2}$). In the centers of action, these heat source/sink correspond to more than 40 % of the atmospheric heat input for this time of

Early Holocene ocean climate of the Eastern Mediterranean

F. Adloff et al.

the year. The obvious connection are the westward Ekman transport of warm surface water and the compensation flow of colder subsurface water. This pattern is restricted to the period, when the Etesian winds are blowing. In the other months, westerly winds are prevailing. The annual mean climatological net air-sea heat exchange shows only a very weak annual mean heat loss in the Western Levantine (Fig. 15), indicating that the heat "piracy" of the Western Levantine is restricted to late spring and summer. In the other months of the year, the Western Levantine is actually exporting heat.

In order to determine, whether the summer heat piracy is a model artefact, we performed the same calculation using net atmospheric heat input from the ERA-Interim Reanalysis averaged over the years 1989–2005 (Berrisford et al., 2009) and the ocean heat content changes calculated from the MEDATLAS temperatures (Fig. 14, right). The results show an even stronger heat piracy (up to $150\,\mathrm{Wm^{-2}}$) around Crete and in the Southeastern Levantine. Additional simulations performed with our ocean model forced with ERA-Interim fluxes have produced similar results (not shown). The difference between modelled and observation-derived estimates can be explained by differences in the Etesian winds. The Etesian winds derived from the global model are essentially blowing from the north (Figs. 11 and 12). In the present-day observations, they also have a westerly component over the Levantine, thus causing the west-east dipole of the model to be somewhat rotated with the strongest part of the upwelling shifted more to the southeast, and the strongest part of the downwelling shifted more to the south. The observed Etesian winds are also slightly stronger, which explains the stronger heat piracy in the observation-based estimate.

During the HIM, the amplified seasonal cycle of surface temperature (which is a direct effect of the insolation forcing) enhances the vertical gradients in near-surface ocean temperature. Together with the Ekman-induced circulation, this stronger seasonality of the insolation cycle could explain the pattern of subsurface temperature changes displayed by the anomalies 9K vs. CTRL (Fig. 9). In the upwelling region of Eastern Levantine, colder subsurface water is upwelled, in the Western Levantine warmer surface water is downwelled, thus causing a positive anomaly of subsurface

temperatures. Additionally, the modelled Etesian winds are found to be increased for both HIM experiments (Fig. 11): a further strengthening of the temperature dipole is thus expected through enhanced Ekman transport.

In the following, the respective contributions of increased Etesian winds and enhanced seasonal cycle of insolation, to subsurface temperature anomaly in Cretan and South Levantine regions are analyzed. For this purpose, three different 100-yr sensitivity experiments are set up, all starting in year 600 of experiment 9K2:

– 9K2-W0 uses the same setup as the 9K2 simulation, but both wind speed and wind stress from CTRL (weaker Etesian winds) are prescribed. With this simulation, the effect from the "full" wind (speed and stress) on the 9K2 climate can be assessed when compared with 9K2, and the effect of the increased thermal forcing alone can be assessed when compared to CTRL.

– CTRL-W9 is similar to CTRL simulation, but we prescribe both wind speed and wind stress from the 9K2 experiment (enhanced Etesian winds). This simulation enlightens the effect of the "full" wind signal (speed and stress) on the CTRL climate when compared with CTRL.

– CTRL-stress9 has the same setup as CTRL-W9, but only the wind stress component from 9K2. This experiment allows to analyze the separate contributions of wind speed and stress through comparison with the simulation CTRL and CTRL-W9.

Figure 16 displays the contribution of different factors to temperature anomalies at different levels of the subsurface. Factors analyzed are (1) the enhanced insolation forcing (9K2-W0 vs. CTRL), (2) the increased Etesian winds on CTRL climate (CTRL-W9 vs. CTRL), and (3) the increased Etesian winds on 9K2 climate (9K2 vs. 9K2-W0). Separate contributions are compared to the total effect from both increased winds and enhanced seasonal cycle of insolation (9K2 vs. CTRL). Figure 17 isolates the effect from both wind components: (1) the enhanced wind stress (CTRL-stress9 vs. CTRL), (2) the enhanced wind speed (CTRL-W9 vs. CTRL-stress9) for selected depths.

The pure effect of the insolation in the 9K2 simulation is dominant in the first model layer (0–12 m), and is responsible for a mean warming of 0.5 K (Fig. 16a). The contribution of enhanced winds induces a mean cold bias of 0.3 K on a CTRL climate (Fig. 16b) and 0.2 K on a 9K2 climate (Fig. 16c). The wind-induced cooling is almost entirely a consequence of the enhanced wind speeds (Fig. 17b), the wind stress effect is small at the surface (Fig. 17a).

In the second layer (12–22 m), the insolation effect is strongly reduced with a warming around 0.2 K in the Cretan and Southwestern Levantine regions and a cooling in Eastern Levantine (Fig. 16e). These patterns are expected in this case, which combines enhanced summer insolation signal and present-day winds: the water downwelled in Southwestern Levantine is warmer, leading to warmer pattern, and the subsurface water upwelled in Eastern Levantine is colder, leading to colder pattern. In this second layer, the main effect of stronger Etesian winds is still a cooling (Fig. 16f and g), however, a warming up to 0.2 K becomes noticeable in the South Levantine area on 9K2 climate (Fig. 16g).

From the third ocean layer (22–32 m) toward greater depth, the remaining cooling from the winter is prevailing, explaining the cold anomalies displayed for the insolation effect (Fig. 16i and m). The effect from the increased wind becomes strong from 22 m on: on CTRL climate, Southwestern Levantine shows warm anomalies up to 0.5 K in 22–32 m layer (Fig. 16j) and up to 0.8 K in 32–42 m layer (Fig. 16n), Eastern Levantine cooling reached the value of 0.6 K in both layer. On 9K2 climate, the warming induced by increased winds in Southwestern Levantine is 0.2 K stronger than on CTRL climate (Fig. 16k vs. j, and Fig. 16o vs. n).

The enhanced wind stress leads to enhanced Ekman transport, namely stronger downwelling in Southwestern Levantine and stronger upwelling in Eastern Levantine. The effect from the increased wind stress becomes strong below 22 m: warm anomalies up to 0.5 K in 22–32 m layer (Fig. 17c) appear in Southwestern Levantine, and the cooling reaches values up to 0.6 K in Eastern Levantine. Linked to the enhanced Ekman transport, both patterns persist down to 250 m depth. A cooling pattern is

also simulated southeast of Crete because the enhanced wind stress of 9K2 is slightly rotated to the east. This induces (1) a downwelling of warm water restricted to the extreme Southwestern Levantine (vs. Western Levantine in CTRL, see Fig. 13), (2) an upwelling of cold water slightly extended to the west (vs. CTRL). Both changes

5 contribute to the cold pattern observed southeast of Crete, while looking the effect of enhanced wind stress (Fig. 17c).

The enhanced wind speed induces a stronger mixing at the top of the water column leading to stronger heat transfer from the sea surface toward subsurface. The sea surface is thus losing heat, leading to cold anomalies at the top of the water column

10 (Fig. 17b). The subsurface layer shows warm anomalies up to 0.5 K due to heat gain through higher transfer to subsurface (Fig. 17d). However, this warm pattern driven by enhanced wind speed is localized southeast of Crete and in the Eastern Levantine, damping in both areas the cooling signal from the enhanced wind stress.

In general the wind effects become stronger when acting on a temperature distri-

15 bution with enhanced vertical gradients. This becomes obvious when comparing the respective panels with wind effects on CTRL and 9K2 basis state. Thus the nonlinear effects between the two mechanisms (stronger seasonal cycle and stronger Etesian winds) are amplifying the temperature signal.

When all effects are combined, the total results to a subsurface warming pattern

20 around Crete and in Southwestern Levantine in the 12–22 layer (Fig. 16h). The warming around Crete vanishes for the 22–32 m layer (Fig. 16l), because of the prevailing cooling from the insolation signal (Fig. 16i). Only the warming in Southwestern Levantine (induced by enhanced downwelling of warm water) is strong enough to prevail in the layers 22–32 m (Fig. 16l) and 32–42 m (Fig. 16p).

25 From this analysis, we conclude that general anomalous heat accumulation happens in the region south of Crete for both CTRL (Fig. 14) and paleo-simulations in summer, and can be attributed to Ekman transport. However, during the HIM, the combination of (1) enhanced downwelling in Southwestern Levantine, (2) enhanced mixing around Crete; both related to increased Etesian winds; and (3) enhanced thermal forcing,

Title Page

Abstract | Introduction

Conclusions | References

Tables | Figures

◄ | ►

◄ | ►

Back | Close

Full Screen / Esc

Printer-friendly Version

Interactive Discussion

are driving together stronger surface heat transfer to the subsurface during summer in the Cretan/Southwestern Levantine region and are thus responsible for the simulated warm subsurface anomaly pattern.

4.3.3 The SST reconstructions

The transfer function used to reconstruct the paleo-SST is based on census counts of 23 species of planktonic foraminiferal species in 274 core tops, 145 from the Mediterranean and 129 from the Atlantic (Hayes et al., 2005). The data are calibrated to seasonal (JFM and JAS) and annual mean SST values at 10 m water depth from the observational dataset WOA (Levitus et al., 1998). The transfer function method based on "artificial neural networks" is described in Hayes et al. (2005).

Based on ^{14}C data, oxygen isotope stratigraphy, biostratigraphy or a combination of those, the Holocene Insolation Maximum interval has been identified in 33 Mediterranean sediment cores as an interval between approximately 9.5 and 8.5 ky BP. Only samples occurring within this interval as identified by the individual age models were considered. Faunal counts were collated with the same procedure as for the core-top samples. SST reconstructions were averaged throughout each Holocene Insolation Maximum Interval for each core.

The full data and discussion of the proxy resulted are presented in a companion paper by Kucera et al. (2011).

4.3.4 SST model-proxy comparison

In this section, we compare the modelled SST with the SST reconstructions. We first compare the absolute SST values of the 9 ky BP simulations with the 9.5–8.5 ky BP reconstructed SST. Annual, summer (JAS) and winter (JFM) temperatures are analyzed. The comparison was performed for both HIM simulations 9K1 and 9K2.

Figure 18 (1st row) displays the model/reconstruction comparison of the annual mean SST for 9 ky BP. The 9K1 simulation, which only considers the change in solar forcing, yields too warm SST in comparison with the reconstructions. In contrast, the

SST predicted by the model in the 9K2 simulation match relatively well with the reconstructions because the 9K2 simulation takes also into account the cooling effect of the glaciers and the reduced atmospheric CO_2 concentration, which leads to SST 1 K colder than for the 9K1 simulation. The model-data discrepancies of the 9K1 simulation are mainly located in the Central Ionian, with a warm bias of 1 K. As for the CTRL simulation, this bias may be linked to the Atlantic-Ionian jet travelling too far north in the model.

The Aegean and the Adriatic are two regions difficult to simulate at our resolution due to their size and small-scale processes acting over these areas, among these are katabatic winds, which are not resolved adequately by the coarse global model. This may explain the up to 5 K discrepancies encountered. Those inconsistencies are found for winter and summer in both regions. Furthermore, the two temperature reconstructions available for the Adriatic differ strongly so that it is difficult to extract a clear signal from the observations for this region. The modelled SST fall between both reconstructed SST values. The simulated winter SST (Fig. 18, 2nd row) match well with the reconstructed winter SST for both simulations: the biases do not exceed 1 K except for the Aegean. The major disagreement between model and proxy data is restricted to summer SST (Fig. 18, 3rd row): both HIM experiments show a warm bias with summer SST errors in excess of 4 K in average for the 9K1 simulation and 3 K for the 9K2 simulation. Again, except for the enclosed Aegean and Adriatic Seas, the major discrepancies are found in the Central Ionian and in the Tyrrhenian Sea.

Two points are important to notice at this stage of the analysis: the simulated temperature signal decreases very quickly with depth in the upper part of the water column during the summer season, due to strong stratification (Fig. 8). Moreover, the foraminifera used for the SST reconstructions do not live at the surface; they inhabit the entire water column all the way down to sub-thermocline depths (Bé et al., 1977; Schiebel and Hemleben, 2005). They are thus likely to record subsurface temperatures, which are colder than the surface temperature in summer. Therefore we also considered subsurface temperature for our comparison (see below).

Early Holocene ocean climate of the Eastern Mediterranean

F. Adloff et al.

To evaluate how model and reconstructions depict differences between the HIM and the present-day, we compare the 9K1/9K2 simulations with the CTRL simulation, and the time slice 9.5–8.5 ky BP of reconstructed SST with pre-1998 instrumental mean SST. The differences allow us to check the ability of the model to reproduce the changes between the HIM and the present-day ocean state, without being affected by the internal model discrepancies that may have an impact on the absolute values. The reconstructed SST anomalies (Fig. 19) reveal strong spatial patterns of the signal. The annual and summer reconstructed SST anomalies (Fig. 19, 1st and 3rd rows) show a strong warming around the Cretan region and a cooling of middle Ionian, the Tyrrhenian and Eastern Levantine. The patterns are the same for summer and annual SST anomalies, but the amplitude of the signal is much stronger in summer. Indeed, the reconstructed winter SST anomalies (Fig. 19, 2nd row) show a cooling, except for the Cretan region, where the anomalies are almost zero and the region around Sicily which even displays a light warming: this winter signal dampens the stronger summer signal and explains the smoother gradient for the annual SST reconstructions. Concerning the model ability to reproduce these spatial anomaly patterns, the model results are not consistent with the reconstructions. Whereas the tripole pattern is somewhat imaged by the 9K1 simulation for the annual SST anomalies, the 9K2 simulation is again consistently too cold. For the summer SST anomalies, the 9K1 experiment shows a rather homogeneous warming but hardly any cooling of the middle Ionian and the Tyrrhenian. The 9K2 experiment shows a much weaker warming and is able to reproduce an enhanced warming pattern around Crete. The modelled winter SST anomalies do not show the warming around Sicily, and the 9K2 experiment simulates a far too strong cooling over the entire basin.

The strong depth dependency of both annual and summer temperature signals leads us to consider a new depth-integrated approach of interpreting SST derived from foraminifera census data. Moreover, the temperature anomaly patterns recorded by the reconstruction closely resemble the patterns recorded at subsurface depth in our simulation, as shown in the Sect. 4.3.2. This strengthens our motivation to test an

approach which integrates subsurface temperature to validate model data with temperature reconstructions from proxy data.

4.3.5 A depth-integrated approach for model-proxy comparison of upper-ocean temperature

In this section, we propose a new approach for the comparison of surface temperature signal between model simulations and reconstructions based on planktonic foraminifera in a setting where there are reasons to believe that the vertical water column structure in the past has had no modern analog.

We consider temperatures averaged over a larger depth interval for our model/proxy comparison instead of restricting it to a pure SST signal. As an example, we choose to integrate the temperature over the depth interval between 0 and 30 m (henceforth T_{0-30}), where the vertical temperature gradient is strongest.

The proxy temperatures, however, are in a strict sense only valid for 10 m depth. As no core top/piston core estimates of the pre-industrial climate exist, anomalies versus climatologies for this depth have been used. It is obvious, that this is not an adequate approach for comparison with T_{0-30} signals. The present-day climatology for T_{0-30} can easily be calculated from the same climatology, but the proxy data should have been estimated with T_{0-30} as base too, which is beyond the scope of this paper. As a simple approximation, we calculate a linear regression between T_{10}, which has been originally used to fit the proxy data, and T_{0-30} from the World Ocean Atlas dataset. Only data from the Mediterranean and the North Atlantic (between 30° and 50° North and east from −20° longitude) have been used. We apply this relation subsequently to the reconstruction data and get a new set of reconstructions for T_{0-30}. The following functions are applied: $T_{0-30} = 0.97\,T_{10} + 0.29$ for annual temperatures, $T_{0-30} = 0.99\,T_{10} + 0.015$ for winter and $T_{0-30} = 0.9\,T_{10} + 1.45$ for summer. The R^2 is higher than 0.977 for all three scalings. The root mean square deviation (RMSD) of the obtained T_{0-30} is 0.41 K for summer, 0.02 for winter and 0.17 for annual mean. In winter, the mixed layer depth is in general deeper than 30 m and the vertical temperature gradient is small. For this

Title Page

Abstract | Introduction

Conclusions | References

Tables | Figures

|◄ | ►|

◄ | ►

Back | Close

Full Screen / Esc

Printer-friendly Version

Interactive Discussion

season, the results for T_{0-30} are not substantially different from the results for T_{10}. Thus the results will only be discussed for summer and annual mean.

The new model/proxy comparison for the absolute 0–30 m averaged temperature is displayed in Fig. 20.

The new comparison shows a great improvement, especially for the summer season where the strongest discrepancies were found in the previous strict SST comparison. For both simulations, the biases between modelled and reconstructed 0–30 m temperatures are generally below ±1 K, for summer and annual mean.

Fig. 21 displays the new comparison for the 0–30 m averaged temperature anomalies (9 ky BP vs. CTRL) simulated by the model and the one recorded by the proxy indicators.

The reconstructed 0–30 m averaged summer temperature anomalies do show a tripole (Fig. 21, 2nd row). In the Tyrrhenian, the Central Ionian and the Eastern Levantine, the cooling signal is less pronounced than with the strict SST reconstructions; this is in agreement with the modelled signal of the 9K2 simulation. The cold anomalies simulated by 9K1 in these regions are weak and even missing for the Eastern Levantine. The new T_{0-30} reconstructions show a more homogeneous warming around Crete. This warming is simulated in the 9K1 experiment but the warmest anomalies are located in the Southwestern Levantine. The 9K2 experiment displays a light cooling in the Cretan region and a light warming in the Southwestern Levantine. The model produces the warmest anomalies in the Southwestern Levantine rather than in the Cretan region because the downwelling of warm surface water is simulated too far south. Nevertheless, in few locations, the anomalies (9 ky BP vs. present-day) of estimated 0–30 m temperature reconstructions show a signal which is lower than the RMSD of the estimated summer 0–30 temperature signal (0.41 K). These results should thus be interpreted cautiously.

It is worth to mention that if the modelled Etesian winds had a stronger westerly component, and had their core centered over the East Aegean (as it is recorded by the observations), the downwelling of warm surface water would occur around Crete,

leading to warm subsurface anomalies there rather than in the Southwestern Levantine (as shown in Fig 14, right). This would also improve the agreement between model and proxies, showing a modelled warming more centered around Crete, consistently with the reconstructed signal.

These results confirm the hypothesis that the model/proxy comparison should involve a temperature signal integrated over a wider range of subsurface depth, consistent with the range of living depths of the planktonic foraminifera used, instead of restricting to a SST signal. Ideally, a new transfer function should be used to perform the reconstructions, taking into account an integrated temperature signal.

The simulation 9K2 seems to represent an upper-ocean climate somewhat more realistic than the 9K1 simulation which simulates in general a too warm climate, due to the fact that the forcing used for this simulation does neither include the cooling effect from the melting glaciers nor from the lower $p\text{CO}_2$.

5 Conclusions

We have modelled the upper ocean climate of the Eastern Mediterranean for the Holocene Insolation Maximum (9000 yr BP) with a regional OGCM forced by daily atmospheric data derived from global simulations. Two experiments have been carried out: 9K1 with changes in solar forcing only and 9K2 with changes in solar forcing, atmospheric $p\text{CO}_2$ and topography (presence of major ice sheets).

We analyzed the mechanisms responsible for the enhanced subsurface summer warming observed in the Cretan/West Levantine region during the HIM, which is recorded by both the model and proxy data. The drivers of this warming are found to be a combination of (1) enhanced downwelling (due to stronger Ekman transport) and wind mixing, due to strengthened Etesian winds, and (2) enhanced vertical temperature gradient due to the stronger seasonal cycle in the Northern Hemisphere. Together, these processes induce a stronger heat transfer from the surface to the subsurface

during late summer in the Western Levantine and are responsible for the heat piracy simulated in this region.

We used SST reconstructions from planktonic foraminifera assemblages to validate our HIM simulations, but found it necessary to integrate modelled SST over a depth range of 0–30 m to account for variable habitat depth. Our depth-integrated approach strongly improved the agreement between the reconstructions and the modelling results, although the significance of the results can be discussed only in few core locations. The transfer function should be newly calculated for temperature integrated over a depth range including subsurface.

Because the 9K1 global simulation from which the atmospheric forcing was derived neglects the ice sheets, 9K1 was generally too warm. As the 9K2 simulation is more realistic, it will be used in a future study to perform perturbation experiments in order to simulate stagnating deep water and assess the plausible physical mechanisms responsible for the sapropel S1 formation.

References

Aksu, A. E., Hiscott, R. N., Yasar, D., Isler, F. I., and Marsh, S.: Seismic stratigraphy of Late Quaternary deposits from the Southwestern Black Sea shelf: evidence for non-catastrophic variations in sea-level during the last similar to 10,000 yr, Mar. Geol., 190, 61–94, 2002. 1461

Andersson, A., Bakan, S., Fennig, K., Grassl, H., Klepp, C., and Schulz, J.: Hamburg Ocean

Atmosphere Parameters and Fluxes from Satellite Data – HOAPS-3 – monthly mean., World Data Center for Climate, doi:10.1594/WDCC/HOAPS3_MONTHLY, 2007. 1468

Astraldi, M., Gasparini, G. P., Sparnocchia, S., Moretti, M., and Sansone, E.: The characteristics of the water masses and the water transport in the Sicily Strait at long time scales, Bulletin de l'Institut Oceanographique, Monaco, 95–115, 1996. 1465

Baschek, B., Send, U., Lafuente, J. G., and Candela, J.: Transport estimates in the Strait of Gibraltar with a tidal inverse model, J. Geophys. Res.-Oceans, 106, 31033–31044, 2001. 1465

Bé, A. W. H., Jongebloed, W. L., and McIntyre, A.: X-ray microscopy of recent planktonic foraminifera., J. Paleontol., 43, 1384–1396, 1977. 1478

Berrisford, P., Dee, D., Fielding, K., Fuentes, M., Kallberg, P., Kobayashi, S., and Uppala, S.: The ERA-Interim Archive. ERA Report Series No. 1, Tech. rep., ECMWF: Reading, UK, available at: www.ecmwf.int/publications, 2009. 1473

Béthoux, J. P.: Budgets of the Mediterranean Sea – their dependance on the local climate and on the characteristics of the Atlantic waters, Oceanol. Acta, 2, 157–163, 1979. 1468

Bigg, G. R.: An ocean general-circulation model view of the glacial mediterranean thermohaline circulation, Paleoceanography, 9, 705–722, 1994. 1459, 1460, 1464

Brody, L. R. and Nestor, M. J. R.: Regional forecasts for the Mediterranean Basin, Tech. Rep. 80–10, Naval Environmental Prediction Research Facility, Monterey, California, USA, 1985. 1472

Bryden, H. L. and Kinder, T. H.: Steady 2-layer exchange through the strait of Gibraltar, Deep-Sea Res., 38, S445–S463, 1991. 1465, 1468

Bryden, H. L., Candela, J., and Kinder, T. H.: Exchange through the strait of Gibraltar, Prog. Oceanogr., 33, 201–248, 1994. 1465, 1468

Cramp, A. and O'Sullivan, G.: Neogene sapropels in the Mediterranean: a review, Mar. Geol., 153, 11–28, 1999. 1459

D'Ortenzio, F., Iudicone, D., de Boyer Montegut, C., Testor, P., Antoine, D., Marullo, S., Santoleri, R., and Madec, G.: Seasonal variability of the mixed layer depth in the Mediterranean Sea as derived from in situ profiles, Geophys. Res. Lett., 32, L12605, doi:10.1029/2005GL022463, 2005. 1465

Garzoli, S. and Maillard, C.: Winter circulation in the Sicily and Sardinia straits region, Deep-Sea Res., 26, 933–954, 1979. 1465

Hayes, A., Kucera, M., Kallel, N., Sbaffi, L., and Rohling, E. J.: Glacial Mediterranean sea

Early Holocene ocean climate of the Eastern Mediterranean

F. Adloff et al.

Title Page

Abstract | Introduction

Conclusions | References

Tables | Figures

|◀ | ▶|

◀ | ▶

Back | Close

Full Screen / Esc

Printer-friendly Version

Interactive Discussion

surface temperatures based on planktonic foraminiferal assemblages, Quaternary Sci. Rev., 24, 999–1016, 2005. 1477

Kalnay, E., Kanamitsu, M., Kistler, R., Collins, W., Deaven, D., Gandin, L., Iredell, M., Saha, S., White, G., Woollen, J., Zhu, Y., Chelliah, M., Ebisuzaki, W., Higgins, W., Janowiak, J., Mo, K. C., Ropelewski, C., Wang, J., Leetmaa, A., Reynolds, R., Jenne, R., and Joseph, D.: The NCEP/NCAR 40-year reanalysis project, B. Am. Meteorol. Soc., 77, 437–471, 1996. 1463

Kucera, M., Rohling, E. J., Hayes, A., Hopper, L. G. S., Kallel, N., Buongiorno Nardelli, B., Adloff, F., and Mikolajewicz, U.: Sea surface temperature of the Mediterranean Sea during the early Holocene insolation maximum, Clim. Past, in preparation, 2011. 1460, 1477, 1506, 1507, 1508, 1509

Levitus, S., Boyer, T. P., Conkwright, M., Johnson, D., O'Brian, T., Antonov, J., Stephens, C., and Gelfield, R.: Introduction. World Ocean Database 1998, Vol. 1, NOAA Atlas NESDIS 18, 346 pp., 1998. 1464, 1466, 1477

Ludwig, W., Dumont, E., Meybeck, M., and Heussner, S.: River discharges of water and nutri-ents to the Mediterranean and Black Sea: major drivers for ecosystem changes during past and future decades?, Prog. Oceanogr., 80, 199–217, 2009. 1467

Marsland, S. J., Haak, H., Jungclaus, J. H., Latif, M., and Roske, F.: The Max-Planck-Institute global ocean/sea ice model with orthogonal curvilinear coordinates, Ocean Model., 5, 91–127, 2003. 1461

MEDAR-Group: MEDATLAS 2002 Database, Cruise Inventory, observed and analyzed data of temperature and bio-chemical parameters, IFREMER Edition (4 CDRom), 2002. 1466

Meijer, P. Th. and Dijkstra, H. A.: The response of Mediterranean thermohaline circulation to climate change: a minimal model, Clim. Past, 5, 713–720, doi:10.5194/cp-5-713-2009, 2009. 1460, 1464

Meijer, P. T. and Tuenter, E.: The effect of precession-induced changes in the Mediterranean freshwater budget on circulation at shallow and intermediate depth, J. Marine Syst., 68, 349–365, 2007. 1459, 1464

Mercone, D., Thomson, J., Croudace, I. W., Siani, G., Paterne, M., and Troelstra, S.: Duration of S1, the most recent sapropel in the Eastern Mediterranean Sea, as indicated by accelerator mass spectrometry radiocarbon and geochemical evidence, Paleoceanography, 15, 336–347, 2000. 1459

Meteorological-Office: Weather in the Mediterranean, Vol. I, General Meteorology, H.M.S.O.

London. 2nd edn., 1962. 1472

Mikolajewicz, U.: Modeling Mediterranean Ocean climate of the Last Glacial Maximum, Clim. Past, 7, 161–180, doi:10.5194/cp-7-161-2011, 2011. 1459, 1460, 1461, 1464

Mikolajewicz, U., Groger, M., Maier-Reimer, E., Schurgers, G., Vizcaino, M., and Winguth, A. M. E.: Long-term effects of anthropogenic CO_2 emissions simulated with a complex earth system model, Clim. Dynam., 28, 599–631, 2007. 1462

Myers, P. G. and Rohling, E. J.: Modeling a 200-yr interruption of the Holocene Sapropel S-1, Quaternary Res., 53, 98–104, 2002. 1459, 1464

Myers, P. G., Haines, K., and Rohling, E. J.: Modeling the paleocirculation of the Mediterranean: the last glacial maximum and the Holocene with emphasis on the formation of sapropel S-1, Paleoceanography, 13, 586–606, 1998. 1459, 1464

Peltier, W. R.: Global glacial isostasy and the surface of the ice-age earth: the ice-5G (VM2) model and grace, Annu. Rev. Earth Pl. Sc., 32, 111–149, 2004. 1461, 1462

Pinardi, N. and Masetti, E.: Variability of the large scale general circulation of the Mediterranean Sea from observations and modelling: a review, Palaeogeogr. Palaeocl., 158, 153–174, 2000. 1465, 1466

Roeckner, E., Bäuml, G., Bonaventura, L., Brokopf, R., Esch, M., Giorgetta, M., Hagemann, S., Kirchner, I., Manzini, L. K. E., Rhodin, A., Schlese, U., Schulzweida, U., and Tompkins, A.: The atmospheric general circulation model ECHAM5, Tech. Rep. 349, Max Planck Institute for Meteorology, Hamburg, 2003. 1462

Rohling, E. J.: Review and new aspects concerning the formation of Eastern Mediterranean sapropels, Mar. Geol., 122, 1–28, 1994. 1459

Rohling, E. J. and Hilgen, F. J.: The eastern mediterranean climate at times of sapropel formation – a review, Geol. Mijnbouw, 70, 253–264, 1991. 1459

Rossignol-Strick, M.: African Monsoons, an immediate climate response to orbital insolation, Nature, 304, 46–49, 1983. 1459

Ryan, W. B. F., Pitman, W. C., Major, C. O., Shimkus, K., Moskalenko, V., Jones, G. A., Dimitrov, P., Gorur, N., Sakinc, M., and Yuce, H.: An abrupt drowning of the Black Sea shelf, Mar. Geol., 138, 119–126, 1997. 1461

Schiebel, R. and Hemleben, C.: Modern planktic foraminifera, Palaeont. Z., 79, 135–148, 2005. 1478

Schmiedl, G., Kuhnt, T., Ehrmann, W., Emeis, K. C., Hamann, Y., Kotthoff, U., Dulski, P., and Pross, J.: Climatic forcing of Eastern Mediterranean deep-water formation and ben-

Early Holocene ocean climate of the Eastern Mediterranean

F. Adloff et al.

Title Page

Abstract | Introduction

Conclusions | References

Tables | Figures

|◄ | ►|

◄ | ►

Back | Close

Full Screen / Esc

Printer-friendly Version

Interactive Discussion

thic ecosystems during the past 22 000 years, Quaternary Sci. Rev., 29, 3006–3020, 2010. 1470

Simmons, A. S., Uppala, D. D., and Kobayashi, S.: ERA-interim: new ECMWF reanalysis products from 1989 onwards, ECMWF News, 110, 29–35, 2007. 1468

5 Sperling, M., Schmiedl, G., Hemleben, C., Emeis, K. C., Erlenkeuser, H., and Grootes, P. M.: Black Sea impact on the formation of Eastern Mediterranean sapropel S1? Evidence from the Marmara Sea, Palaeogeogr. Palaeocl., 190, 9–21, 2003. 1461

Stanev, E. V. and Peneva, E. L.: Regional sea level response to global climatic change: Black Sea examples, Global Planet. Changes, 32, 33–47, 2002. 1468

10 Tsimplis, M. N. and Bryden, H. L.: Estimation of the transports through the Strait of Gibraltar, Deep-Sea Res. Pt. I, 47, 2219–2242, 2000. 1465

von Storch, H. and Zwiers, F.: Statistical Analysis in Climate Research, Cambridge University Press, Cambridge, 1999. 1463

Vörösmarty, C., Fekete, B., and Tucker, B.: Global River Discharge, 1807–1991, Version. 1.1

15 RivDIS Data set, available at: http://www.daac.ornl.gov from Oak Ridge National Laboratory Distributed Active Archive Center, Oak Ridge, Tennessee, USA, 1998. 1463

Early Holocene ocean climate of the Eastern Mediterranean

F. Adloff et al.

Title Page

Abstract | Introduction

Conclusions | References

Tables | Figures

|◄ | ►|

◄ | ►

Back | Close

Full Screen / Esc

Printer-friendly Version

Interactive Discussion

Table 1. Fresh water budget for the Mediterranean and the Eastern Mediterranean for CTRL, 9K1 and 9K2.

	Mediterranean			Eastern Mediterranean		
	CTRL	9K1	9K2	CTRL	9K1	9K2
P (mm d^{-1})	0.59	0.66	0.60	0.46	0.55	0.48
(m^3 s^{-1})	17 735	19 330	17 471	8141	9347	8276
E (mm d^{-1})	2.83	2.87	2.83	3.05	3.06	3.00
(m^3 s^{-1})	84 803	83 421	82 524	53 591	52 337	51 297
R total (mm d^{-1})	0.35	0.53	0.45	0.21	0.51	0.37
R total (m^3 s^{-1})	10 443	15 535	13 070	3690	8752	6378
R Nile (m^3 s^{-1})	2930	7494	5401	2930	7494	5401
$P + R - E$ (mm d^{-1})	−1.89	−1.68	−1.78	−2.38	−2	−2.15
Net Gib (mm d^{-1})	1.71	1.68	1.78			
(10^6 m^3 s^{-1})	0.051	0.052	0.049			
Net Bos (mm d^{-1})	0.18					
(m^3 s^{-1})	5621					
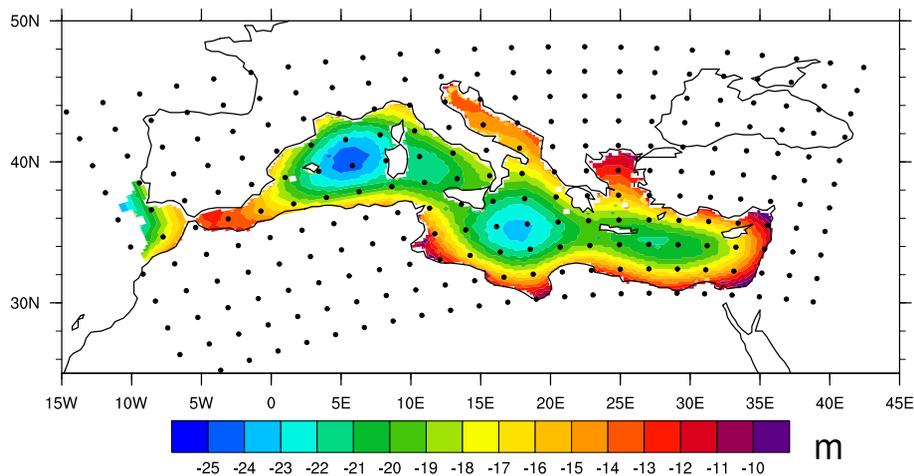
Fig. 1. Topography changes between 9K and CTRL. The superimposed dots represent 1 of each 10 grid box center of the model in each direction.
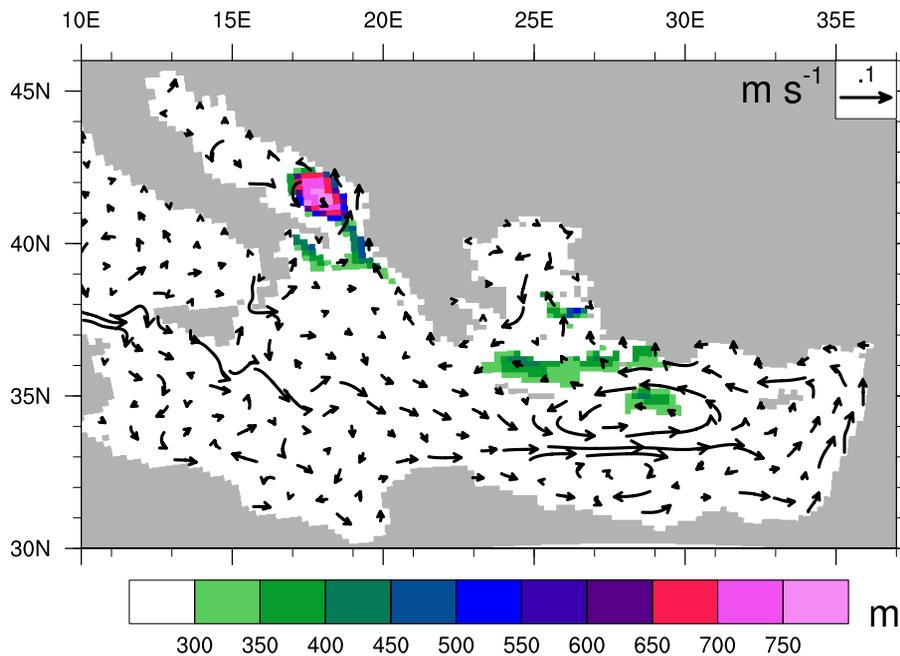
Fig. 2. Modelled March mixed layer depth (colors) and near-surface currents field (arrows) at 27 m depth for CTRL. Only a subset of vectors has been plotted.
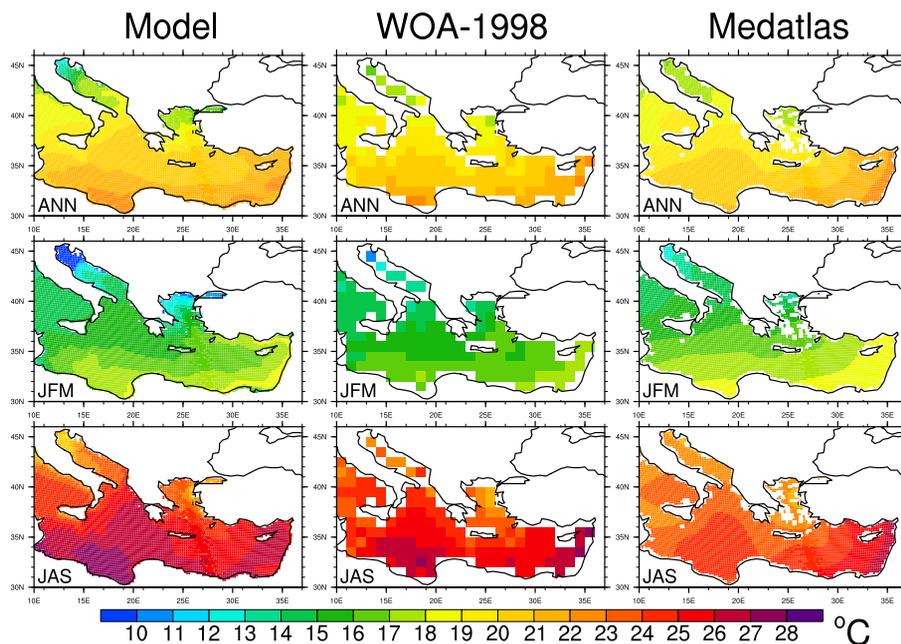
Fig. 3. Annual, winter (JFM) and summer (JAS) SST at 6 m for CTRL (left), World Ocean Data 1998 climatology (middle) and MEDATLAS climatology (right).
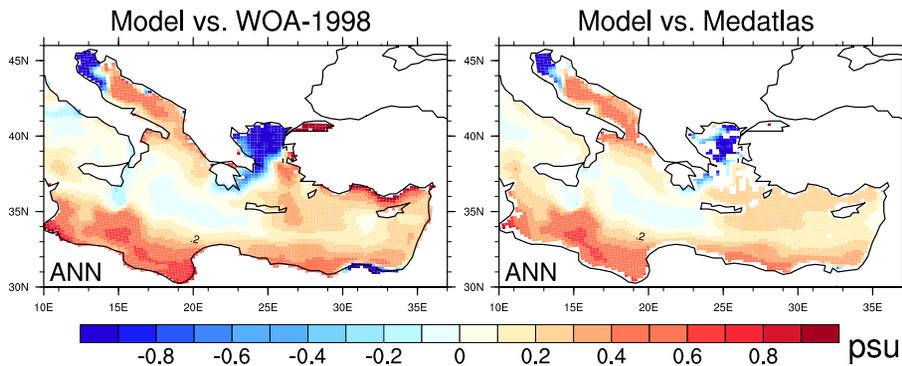
Fig. 4. Annual mean SSS deviations at 6 m, CTRL vs. World Ocean Data 1998 climatology (left) and CTRL vs. MEDATLAS climatology (right).

Full Screen / Esc

Printer-friendly Version

Interactive Discussion
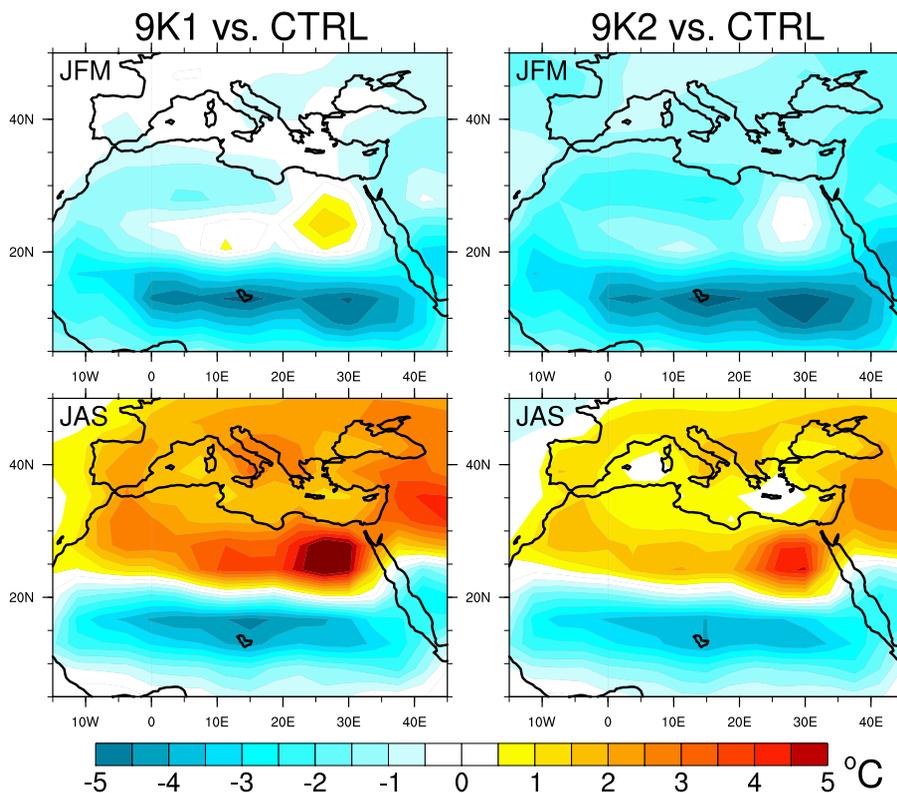
Fig. 5. Anomalies of 2-m temperature for winter (JFM) and summer (JAS) from global simulations, 9K1 vs. CTRL (left) and 9K2 vs. CTRL (right).
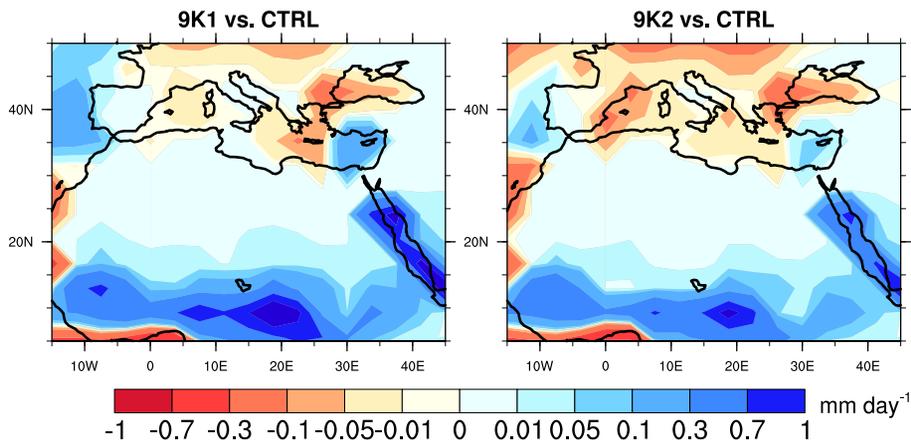
Fig. 6. Annual mean anomalies of $P - E$ from global simulations, 9K1 vs. CTRL (left) and 9K2 vs. CTRL (right).
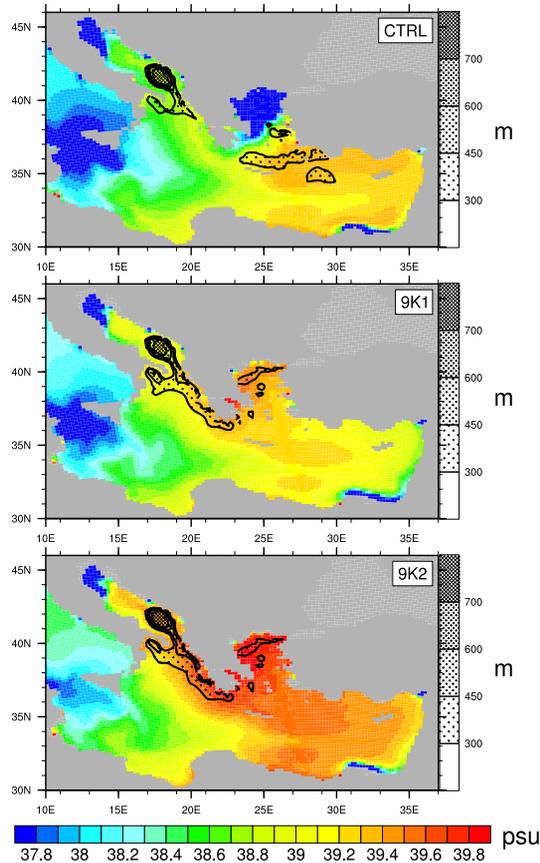
Fig. 7. Annual mean SSS at 6 m depth (colors) and March mixed layer depth (fill patterns), for CTRL (top), 9K1 (middle) and 9K2 (bottom).
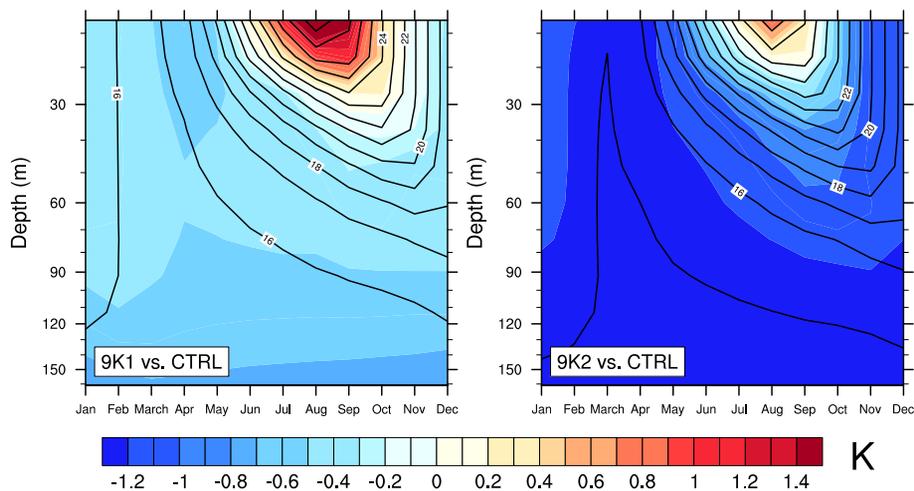
Fig. 8. Anomalies in monthly seasonal cycle of upper ocean temperature averaged over the Eastern Mediterranean, 9K1 vs. CTRL (left) and 9K2 vs. CTRL (right); isolines represent the absolute values in °C for 9K1 (left) and 9K2 (right).
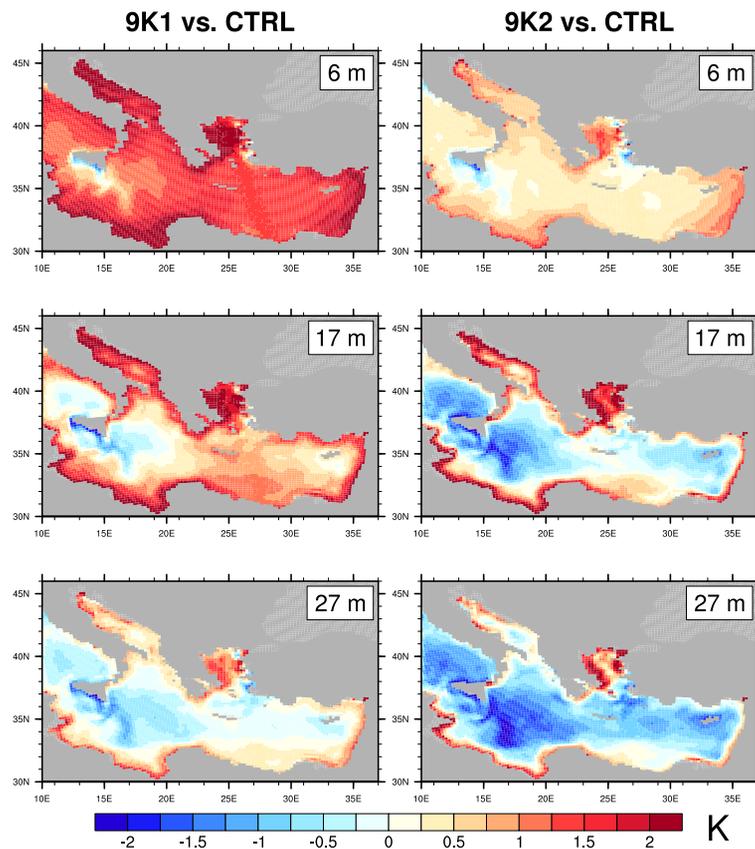
Fig. 9. Anomalies of summer (JAS) temperature at different levels, 9K1 vs. CTRL (left column) and 9K2 vs. CTRL (right column).
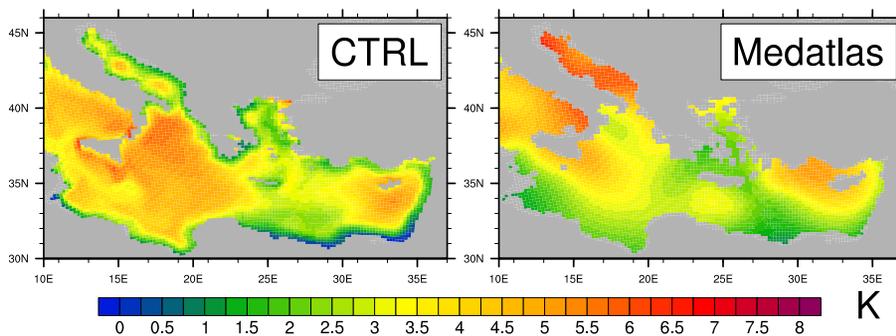
Fig. 10. Summer (JAS) temperature difference between 6 m and 27 m for CTRL and MEDAT-LAS climatology.
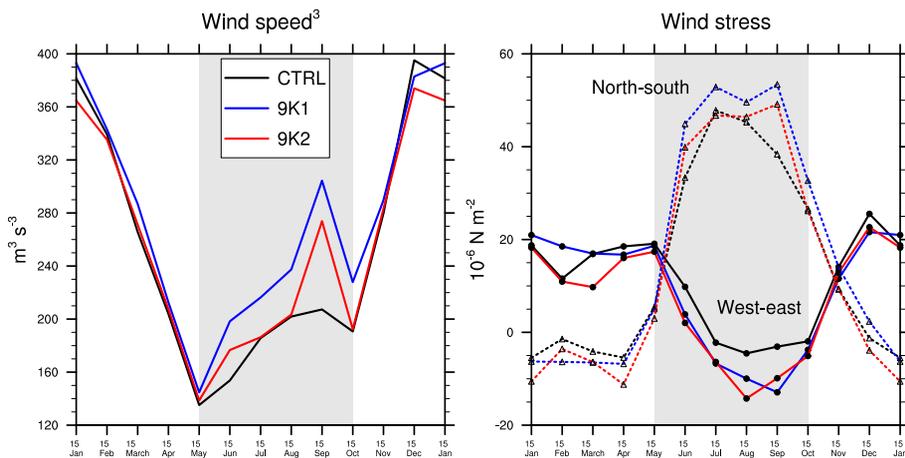
Fig. 11. Monthly climatology of wind components averaged over the Aegean/West Levantine regions for CTRL (black), 9K1 (blue) and 9K2 (red). Left panel shows 10-m wind speed cubed, the cubed value is considered because it is proportional to mixing strength. Right panel shows both west-east and north-south wind stress components. The shading represents the time period, when modelled Etesian winds are active.
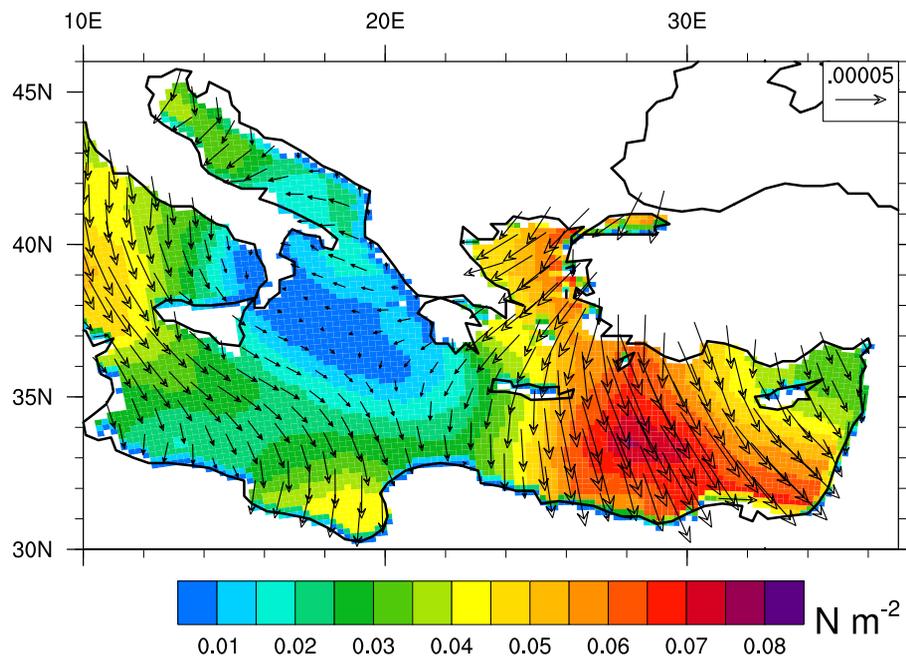
Fig. 12. Mean summer (JAS) wind stress for CTRL.

Early Holocene ocean climate of the Eastern Mediterranean

F. Adloff et al.
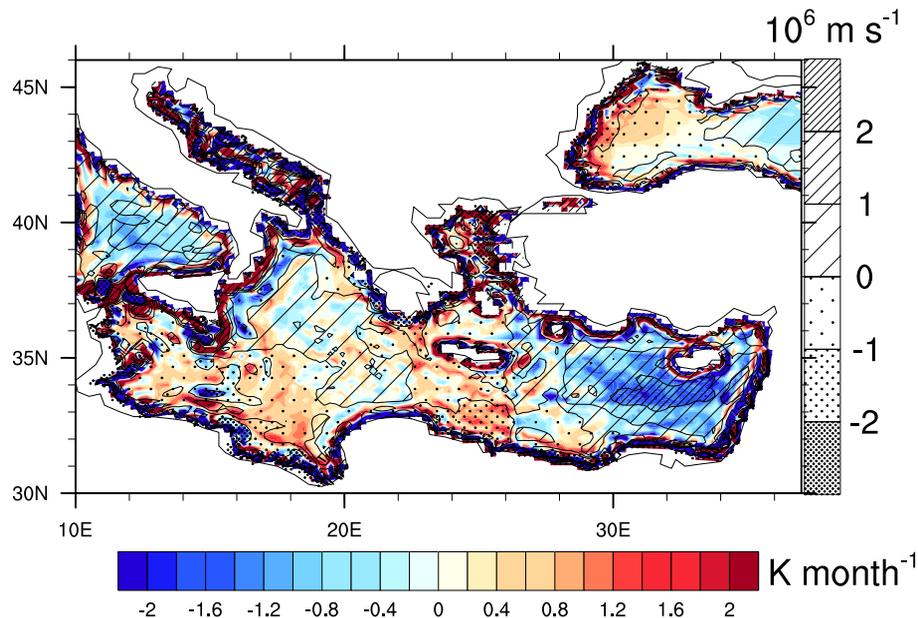
Fig. 13. Temperature change through vertical advection averaged between 12 and 42 m (colours) and vertical velocities (fill patterns, positive values for upward velocities) in July for CTRL.
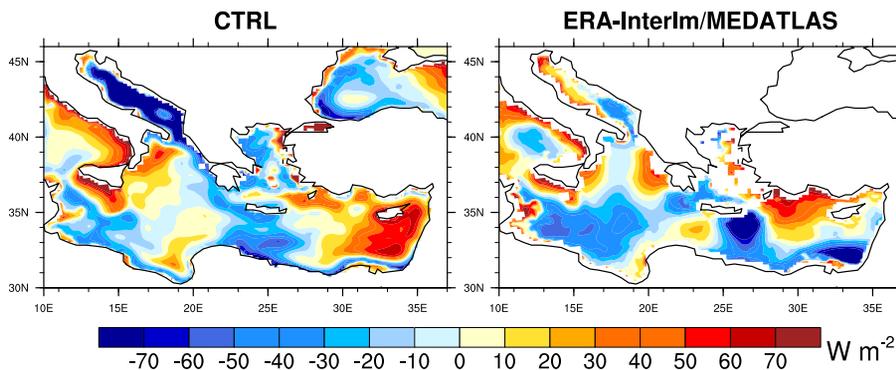
Fig. 14. Difference between the net atmospheric heat input and changes in ocean heat content from 1 May until 30 September. Left panel shows CTRL. Right panel shows differences between net atmospheric heat input from ERA-Interim Reanalysis (averaged over 1989/2005) and changes in ocean heat content from MEDATLAS climatology.

Full Screen / Esc

Printer-friendly Version

Interactive Discussion
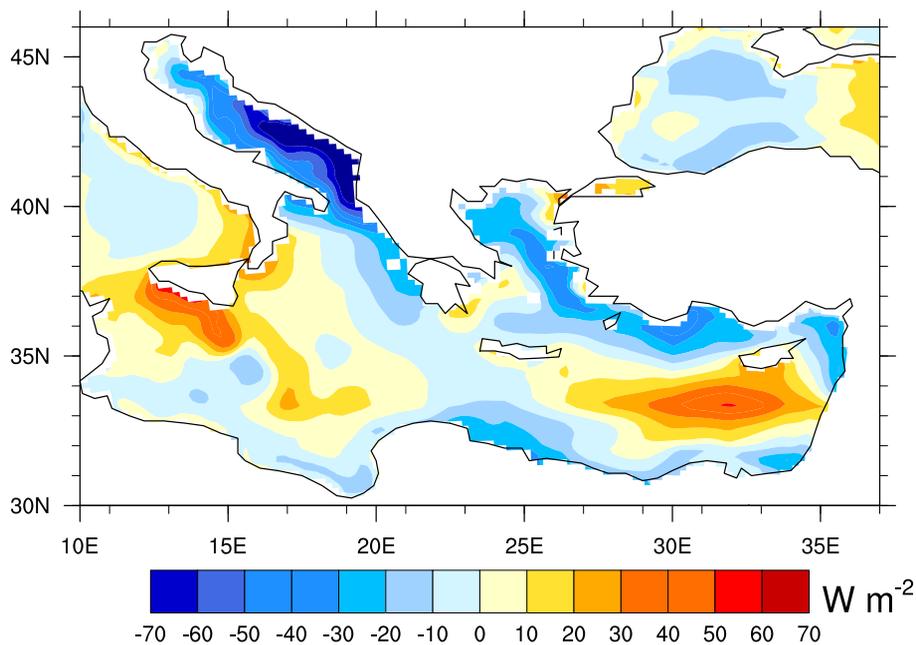
Fig. 15. Annual mean net heat flux at the surface for CTRL.

Fig. 16. Anomalies of temperature for different model layers for summer (JAS). The columns show the isolated effect of insolation forcing (9K2-W0 vs. CTRL), enhanced Etesian winds on CTRL climate (CTRL-W9 vs. CTRL) and on 9K2 climate (9K2 vs. 9K2-W0), as well as the total effect of both factors (9K2 vs. CTRL).
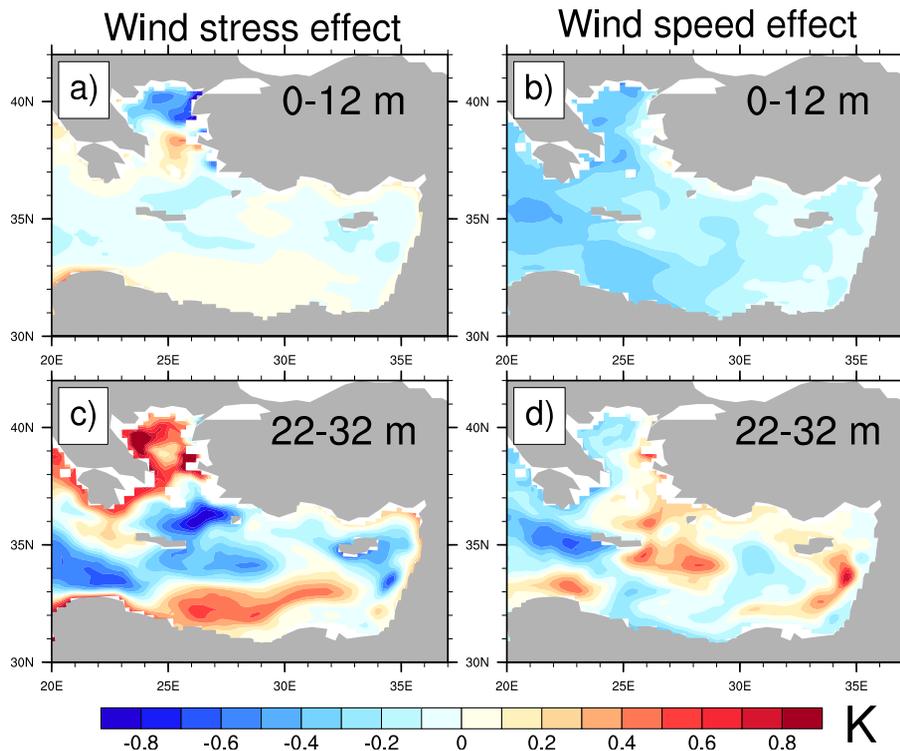
Fig. 17. Anomalies of temperature for different model layers in summer (JAS). The effect of wind stress (CTRL-stress9 vs. CTRL) and wind speed (CTRL-W9 vs. CTRL-stress9) are shown.

Early Holocene ocean climate of the Eastern Mediterranean

F. Adloff et al.

Title Page

Abstract | Introduction

Conclusions | References

Tables | Figures

◀ | ▶

◀ | ▶

Back | Close

Full Screen / Esc

Printer-friendly Version

Interactive Discussion
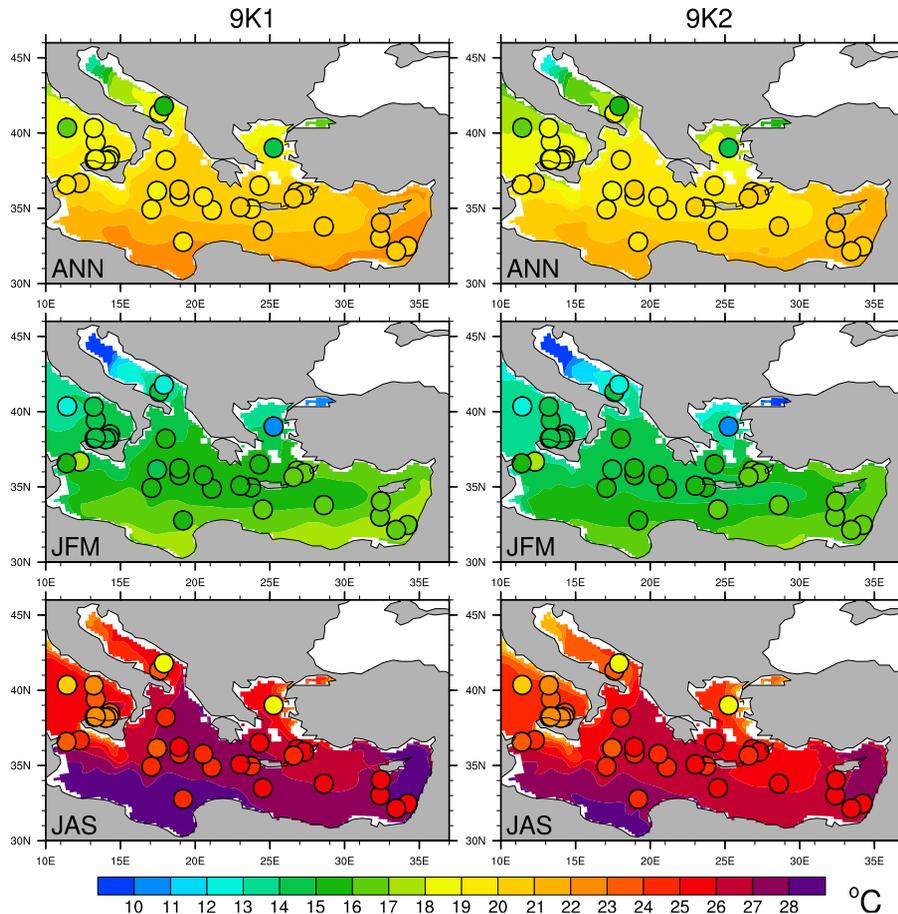
Fig. 18. Annual, winter (JFM) and summer (JAS) SST, reconstructed from proxy data (dots, Kucera et al., 2011) vs. modelled one (background color) for 9K1 (left) and 9K2 (right). 1st row displays annual SST, 2nd row displays winter SST, 3rd row displays summer SST.
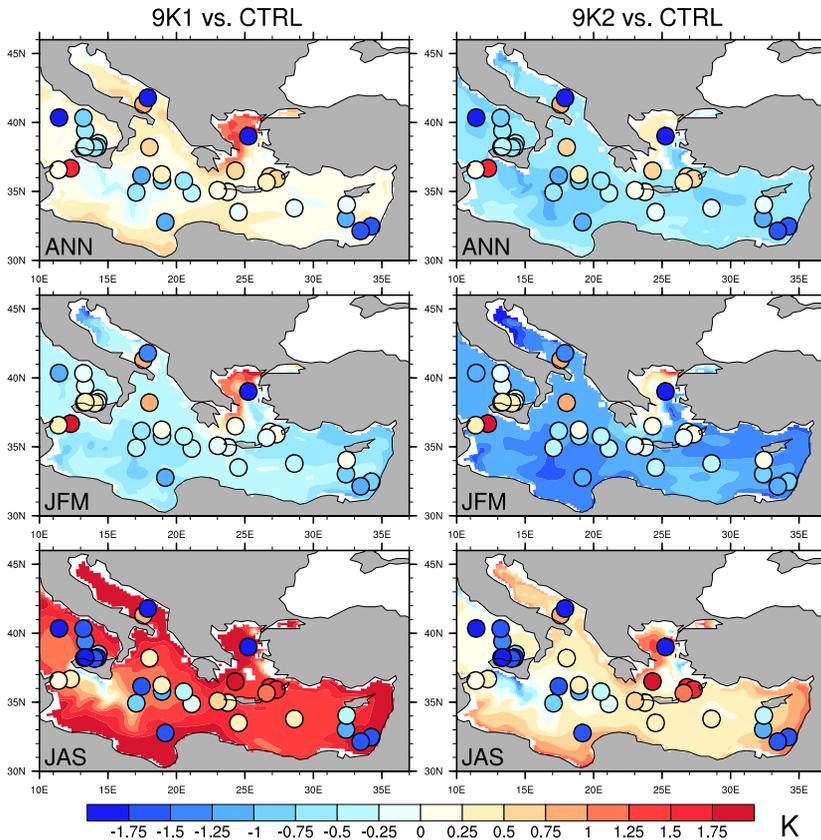
Fig. 19. Annual, winter (JFM) and summer (JAS) SST anomalies, reconstructed from proxy data (dots, Kucera et al., 2011) vs. modelled one (background color) for 9K1 vs. 0K (left) and 9K2 vs. 0K (right). 1st row displays annual SST anomalies, 2nd row displays winter SST anomalies, 3rd row displays summer SST anomalies.

CPD

7, 1457–1509, 2011

Early Holocene ocean climate of the Eastern Mediterranean

F. Adloff et al.

Title Page

Abstract | Introduction

Conclusions | References

Tables | Figures

|◀ | ▶|

◀ | ▶

Back | Close

Full Screen / Esc

Printer-friendly Version

Interactive Discussion
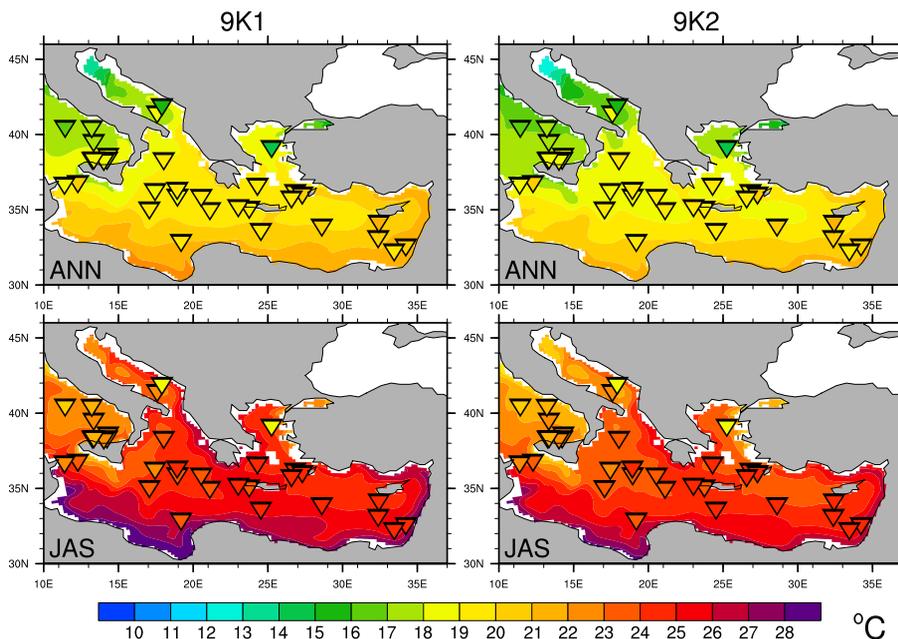
Fig. 20. Annual and summer (JAS) T_{0-30}, calculated from SST reconstructions proxy data (triangles, Kucera et al., 2011) vs. modelled one (background color) for 9K1 (left) and 9K2 (right). 1st row displays annual T_{0-30}, 2nd row displays summer T_{0-30}.
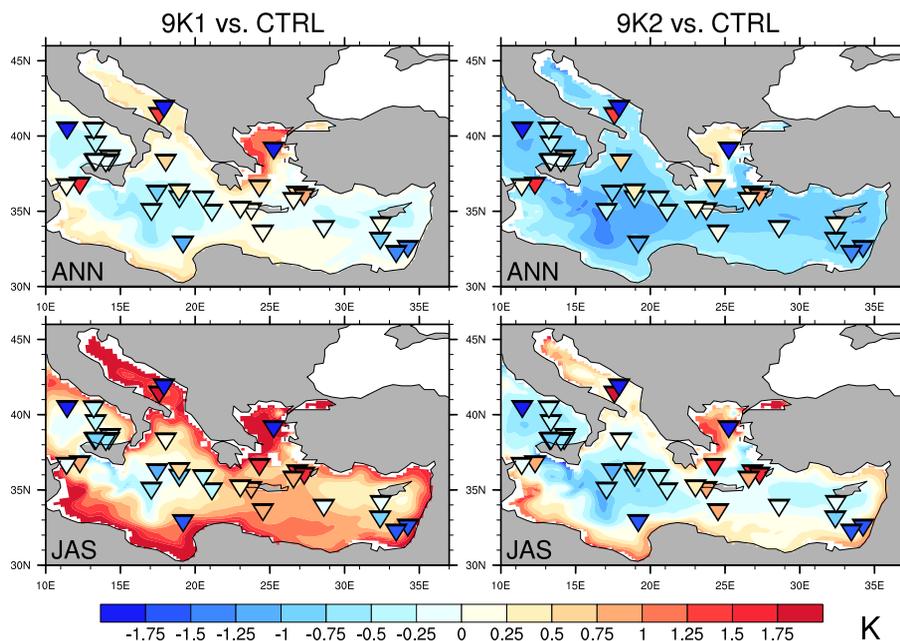
Fig. 21. Annual and summer (JAS) T_{0-30} anomalies, calculated from SST reconstructions from proxy data (triangles, Kucera et al., 2011) vs. modelled one (background color) for 9K1 vs. 0K (left) and 9K2 vs. 0 K (right). 1st row displays annual T_{0-30} anomalies, 2nd row displays summer T_{0-30} anomalies.

Title Page

Abstract | Introduction

Conclusions | References

Tables | Figures

|◄ | ►|

◄ | ►

Back | Close

Full Screen / Esc

Printer-friendly Version

Interactive Discussion